Phase transitions in germanium telluride nanoparticle phase-change materials studied by temperature-resolved x-ray diffraction

Journal Article

Author(s):
Michel, Ann-Katrin U.; Donat, Felix; Siegfried, Aurelia; Yarema, Olesya ⓘD; Fang, Hanbing; Yarema, Maksym ⓘD; Wood, Vanessa ⓘD; Müller, Christoph R.; Norris, David J.

Ann-Katrin U. Michel, Felix Donat, Aurelia Siegfried, Olesya Yarema, Hanbing Fang, Maksym Yarema, Vanessa Wood, Christoph R. Müller, and David J. Norris

Phase transitions in germanium telluride nanoparticle phase-change materials studied by temperature-resolved x-ray diffraction

View Online   Export Citation   CrossMark
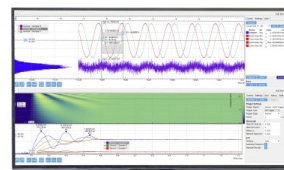
Ann-Katrin U. Michel,[1] [ID] Felix Donat,[2] [ID] Aurelia Siegfried,[1] Olesya Yarema,[3] Hanbing Fang,[1] [ID] Maksym Yarema,[3]
Vanessa Wood,[3] [ID] Christoph R. Müller,[2] [ID] and David J. Norris[1,a) [ID]

AFFILIATIONS

[1]Optical Materials Engineering Laboratory, Department of Mechanical and Process Engineering, ETH Zurich, 8092 Zurich, Switzerland
[2]Laboratory of Energy Science and Engineering, Department of Mechanical and Process Engineering, ETH Zurich, 8092 Zurich, Switzerland
[3]Institute for Electronics, Department of Information Technology and Electrical Engineering, ETH Zurich, 8092 Zurich, Switzerland

[a)]**Author to whom correspondence should be addressed:** dnorris@ethz.ch

ABSTRACT

Germanium telluride (GeTe), a phase-change material, is known to exhibit four different structural states: three at room-temperature (one amorphous and two crystalline, α and γ) and one at high temperature (crystalline, β). Because transitions between the amorphous and crystalline states lead to significant changes in material properties (e.g., refractive index and resistivity), GeTe has been investigated as a phase-change material for photonics, thermoelectrics, ferroelectrics, and spintronics. Consequently, the temperature-dependent phase transitions in GeTe have been studied for bulk and thin-film GeTe, both fabricated by sputtering. Colloidal synthesis of nanoparticles offers a more flexible fabrication approach for amorphous and crystalline GeTe. These nanoparticles are known to exhibit size-dependent properties, such as an increased crystallization temperature for the amorphous-to-α transition in sub-10 nm GeTe particles. The α-to-β phase transition is also expected to vary with size, but this effect has not yet been investigated for GeTe. Here, we report time-resolved x-ray diffraction of GeTe nanoparticles with different diameters and from different synthetic protocols. We observe a non-volatile amorphous-to-α transition between $210\,°C$ and $240\,°C$ and a volatile α-to-β transition between $370\,°C$ and $420\,°C$. The latter transition was reversible and repeatable. While the transition temperatures are shifted relative to the values known for bulk GeTe, the nanoparticle-based samples still exhibit the same structural phases reported for sputtered GeTe. Thus, colloidal GeTe maintains the same general phase behavior as bulk GeTe while allowing for more flexible and accessible fabrication. Therefore, nanoparticle-based GeTe films show great potential for applications such as in active photonics.

Published under license by AIP Publishing. https://doi.org/10.1063/5.0032624

I. INTRODUCTION

Germanium telluride (GeTe) is a metal chalcogenide that exhibits three structural states at room temperature and one state at high temperature.[1,2] The room-temperature states are amorphous GeTe and crystalline rhombohedrally distorted α- as well as orthorhombic γ-GeTe. The high-temperature crystalline cubic phase is known as β-GeTe. While the atoms of such a phase-change material are covalently bonded in its amorphous (A) state, metavalent bonding can be found in the crystalline (C) states.[3] These two types of bonds lead to very different properties. The amorphous state has a relatively low optical reflectivity R_A and high electrical resistivity ρ_A. Upon crystallization, the resistivity decreases by five orders of magnitude with $\rho_A \approx 10^2\,\Omega\,cm$ and $\rho_C \approx 10^{-3}\,\Omega\,cm$.[4] Simultaneously, the reflectance contrast ΔR defined by $[(R_C - R_A)/R_C] \times 100$ is about 43% in the near-infrared spectral range (wavelengths near $1\,\mu m$).[5]

The room-temperature amorphous state of GeTe crystallizes at $T_{C,1} = 185\,°C$.[4] Thermal annealing, optical pulses, or electrical pulses can be used to induce crystallization. However, only laser or electrical pulses allow for the high cooling rates necessary for quenching of the GeTe melt and, thus, re-amorphization. The melting temperature of GeTe is $T_M = 723\,°C$.[6]

The strong property contrast between the non-volatile phases can be exploited for optical data storage and memristive memories.[7,8] The latter are one of the most promising candidates for neuromorphic computing.[9] While ternary and quaternary phase-change materials, such as germanium antimony telluride or silver indium antimony telluride, have been applied in phase-change memories, germanium telluride has gained interest for active photonics.[10–13] Furthermore, GeTe exhibits a ferroelectric transition at about $430\,°C$ (depending on the exact stoichiometry),[14] while doping GeTe with Mn leads to a decrease of this transition temperature by more than a factor of two.[15] Additionally, alloying GeTe with Mn, Pb, or Sn can result in a (ferroelectric) Curie temperature down to $30\,°C$.[16] Moreover, GeTe has recently been identified as a Rashba ferroelectric.[17]

All of the aforementioned applications and effects have been investigated for either epitaxially grown or sputtered GeTe films ranging from several tens of nanometers to several micrometers in thickness. Recently, spatially confined phase-change materials have been studied mainly due to two opportunities. First, nanowires and nanoparticles offer an alternative approach to fabricate films of phase-change material or patterned arrays,[18–21] thereby the purchase of a dedicated expensive equipment (e.g., magnetron sputtering tool) can be avoided. In addition, preformed, high-aspect-ratio voids or patterns can be filled. Second, nanoscale phase-change materials allow for studying size-dependent properties of these compounds. For example, localized surface plasmon resonances have been reported for crystalline GeTe nanoparticles,[22] and a bandgap increase has been observed.[23,24] Furthermore, several studies on the size-dependent shift of the crystallization temperature $T_{C,1}$ have been published, as shown for GeTe in Table I. The listed values for $T_{C,1}$ refer to the transition from the amorphous state to the rhombohedrally distorted α-GeTe and reveal that $T_{C,1}$ increases with decreasing particle diameter d. We also note that the observed crystallization temperature depends not only on the material dimensions but also on the characterization technique. For example, the drop in resistivity associated with crystallization does not require a phase change of the entire GeTe volume; a conductive crystalline channel in the film is sufficient. Another important factor is the applied heating rate ϑ throughout the measurement. A well-known example is the shifted peak temperature to higher T upon increase of ϑ in differential scanning calorimetry (DSC). All of the aforementioned effects have to be taken into account when comparing the values for $T_{C,1}$ and making conclusions about size-dependent effects.

While $T_{C,1}$ has been reported for spatially confined GeTe, the high-temperature crystalline β phase has not been observed for either ultra-small or initially amorphous nanoparticles so far (cf. Table I). Here, we study the reversible crystalline-to-crystalline phase transition from α- to β-GeTe at $T_{C,2}$ and back to the α-phase for sub-10 nm GeTe nanoparticles, which were initially amorphous after synthesis. This is realized by collecting x-ray diffraction

TABLE I. Comparison of crystallization temperatures $T_{C,1}$ and $T_{C,2}$ for different GeTe samples, determined by different characterization methods (XRD—x-ray diffraction, at a synchrotron (s) if applicable, $\rho(T)$—resistivity measurement during heating and cooling, and DSC—differential scanning calorimetry) with varied heating rates given in °C/min. The samples have either been synthesized (approx. spherical particle diameter d) or sputtered (approx. film thickness t). Initially, GeTe has been either in its amorphous (A) or crystalline (C) state. The sputtered thin films are given for reference and separated by a horizontal line.

Size (nm)	$T_{C,1}$ (°C)	$T_{C,2}$ (°C)	Method	ϑ (°C/min)	Ref.
$d_A = 1.8$	400		In situ XRD$_s$	60	20
$d_A = 2.6$	350		In situ XRD$_s$	60	20
$d_A = 3.4$	320		In situ XRD$_s$	60	20
$d_A = 3.5$	340		$\rho(T)$	300–1.800	20
$d_A = 6.0$	227		In situ XRD	7	21
	170		$\rho(T)$		21
	223–240		DSC	2.5–30	21
$d_A = 8.7$	237		DSC	5	25
$d_A = 10.6$	224		DSC	5	25
$d_A = 18.5$	209		DSC	5	25
$d_C = 17.0$		355	In situ XRD$_s$	60	26
$d_C = 100$		360	In situ XRD$_s$	60	26
$d_C = 500$		370	In situ XRD$_s$	60	26
$t_A = 50$	170	350	In situ XRD$_s$	180	27
	175		$\rho(T)$	60	27
$t_A = 80$	185		$\rho(T)$	5	4
$t_A = 100^a$	180		$\rho(T)$	10	28
$t_A = 100^b$	230		$\rho(T)$	10	28
$t_A = 150$	180		$\rho(T)$	10	29

^{a}Surface-oxidized film.
^{b}TaN-capped GeTe film.

(XRD) patterns for repeated heating and cooling cycles of drop-casted particles, which are synthesized in their amorphous state.

II. EXPERIMENTAL METHODS

We prepared colloidal dispersions of amorphous monodisperse GeTe nanoparticles following two different protocols. All studied spherical nanoparticles had a diameter $d < 10\,nm$ since size-dependent crystallization had previously been identified for this size regime (Table I).

A. Nanoparticle synthesis

The syntheses of the amorphous (A-)GeTe nanoparticles followed protocols adapted from Caldwell et al.[20] and reported by Yarema et al.[21]

The first batch was synthesized through a hot-injection route as schematically shown in Fig. 1(a). Anhydrous germanium(II) iodide (GeI$_2$, 163 mg) was dissolved in 2 ml trioctylphosphine (TOP) in a glovebox and stirred overnight. The following day, 2 g of trioctylphosphine oxide (TOPO) was added, and the yellow solution was transferred to a reaction flask that was purged with nitrogen beforehand. After heating the solution to $235\,°C$, $240\,\mu l$
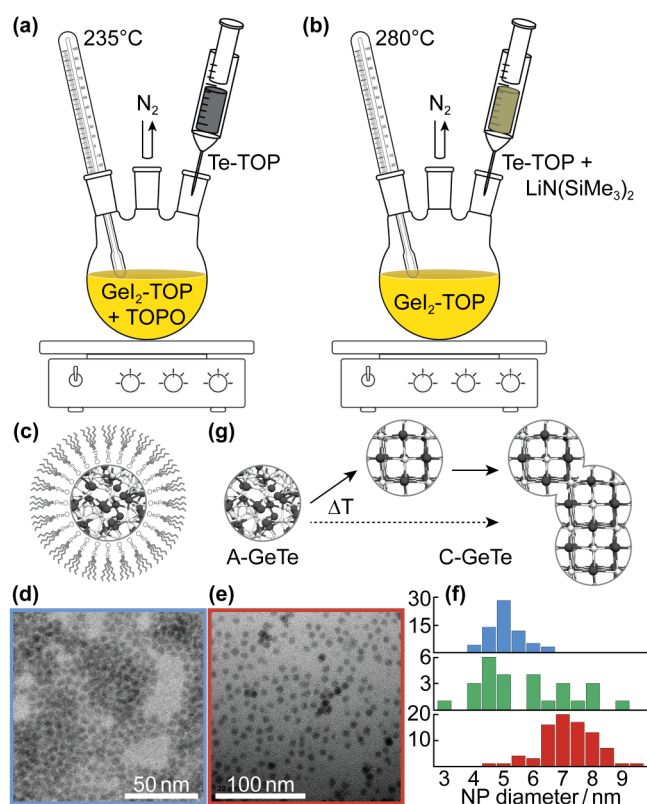
FIG. 1. Sketch of the hot-injection methods 1 (a) and 2 (b) used for the synthesis of amorphous (A) sub-10 nm GeTe nanoparticles, covered by organic ligands, such as trioctylphosphine (TOP), shown in (c). TEM images of the particles with an average diameter of 4.8 nm (d) and 6.9 nm (e) allow for the determination of the particle size distributions shown in (f). The top (blue) and bottom (red) distribution relate to particles from synthesis 2, (b); the middle (green) distribution is for synthesis 1 (a). (g) Heating of the A-GeTe particles with $\Delta T \geq T_{C,1}$ results in crystalline (C) GeTe particles, which are likely to coalesce prior or throughout the crystallization process (dashed and solid arrow, respectively).

dodecanethiol and 30 s later 667 μl 0.75M Te-TOP solution (previously prepared) were injected. About 40 s later, the color of the solution in the flask changed from yellow to dark brown, indicating nucleation of nanoparticles. After 4 min, the reaction was terminated and the flask was cooled rapidly by acetone mist and later, with pressurized air. The crude solution of GeTe nanoparticles was transferred air-free to the glovebox where anhydrous ethanol was added (3:1). The black precipitate was separated by centrifugation (4000 rpm, 10 min) and dispersed in 1 ml anhydrous chloroform. After centrifuging (4000 rpm, 10 min), ethanol was added to the dark brown solution (2:1). Another centrifugation step resulted in a clear liquid and a black precipitate. The latter was dispersed in 1 ml toluene, forming a colloid that remained stable for multiple weeks. We refer to this synthetic protocol below as *synthesis 1*.

The alternative synthetic approach, *synthesis 2*, led to several batches with different GeTe particle sizes. This amide-promoted synthesis is schematically shown in Fig. 1(b) and described in detail in Ref. 21. While the A-GeTe nanoparticles obtained from synthesis 1 were covered by TOP ligands [cf. Fig. 1(c)], the particles from synthesis 2 were covered with an oleate shell.

From transmission electron microscopy (TEM) observations, the average size of each particle synthesis was estimated. The A-GeTe particle size available from synthesis 1 was 5.5 ± 1.6 nm; synthesis 2 provided A-GeTe particles with diameters 4.8 ± 0.6 nm, Fig. 1(d), and 6.9 ± 0.9 nm, Fig. 1(e). It has to be noted that synthesis 2 led to particles with a much narrower size distribution, as visible in Fig. 1(f): the green size distribution refers to the particles from synthesis 1 and the blue and red size distributions refer to the particles from synthesis 2.

Upon annealing, the A-GeTe particles will relax into the crystalline phase if $\Delta T > T_{C,1}$. However, due to the large surface-to-volume ratio of small nanoparticles, coalescence is energetically favorable. Thus, coalescence of sub-10 nm particles has been reported either at temperatures above $T_{C,1}$[21] or at lower temperatures. Thus, it occurs prior or throughout crystallization [cf. Fig. 1(g)].[30]

B. Temperature-dependent x-ray diffraction

Samples were prepared for each particle size by repeated drop casting onto a circular quartz substrate (diameter 1.3 cm). The sample thickness and weight, including the nanoparticles, ligands, and residual solvent, were not determined. However, the sample deposition was conducted with a particle concentration of about 5 mg/ml and an estimated deposited amount of 5 mg. Due to the repeated drop casting of the colloidal dispersions, we expect a densely packed assembly of nanoparticles on the quartz substrate. To avoid oxidation, the colloid was deposited air-free in a nitrogen glovebox. The samples were mounted in an Anton Paar XRK 900 reactor chamber that was purged with nitrogen (flow rate: 200 ml/min, measured at ambient temperature and pressure) throughout the entire measurement. The samples were characterized with a PANalytical Empyrean diffractometer equipped with a X'Celerator Scientific ultrafast line detector and Bragg-Brentano HD incident beam optics. The instrument was operated at 45 kV and 40 mA using Cu Kα radiation (1.540 60 Å). The temperature was measured and controlled in the vicinity of the sample using a type K thermocouple; separate control measurements with a second thermocouple placed at the exact position of the sample indicated that the temperature difference between the two thermocouples was < 5 °C for temperatures $T < 800$ °C.

Figure 2(a) shows the applied temperature curve. The XRD chamber temperature T is plotted as a function of the time t during two heating and cooling cycles. The samples were heated and cooled at a rate of $\vartheta = 10$ °C/min. At each T, the chamber was held for 6 min total, which includes 1 min for equilibration and 5 min for the actual XRD scan.

In the case of bulk stoichiometric compounds, we expect the crystallization of the initial A-GeTe to the α phase. α-GeTe will then remain stable to $T_{C,2} = 357$ °C.[2] Above this temperature, the β phase becomes stable. If GeTe is rich in tellurium (> 50.9%), A-GeTe crystallizes to the γ phase. At elevated temperatures, a γ-to-β transition can be observed.[2] An overview of the crystalline
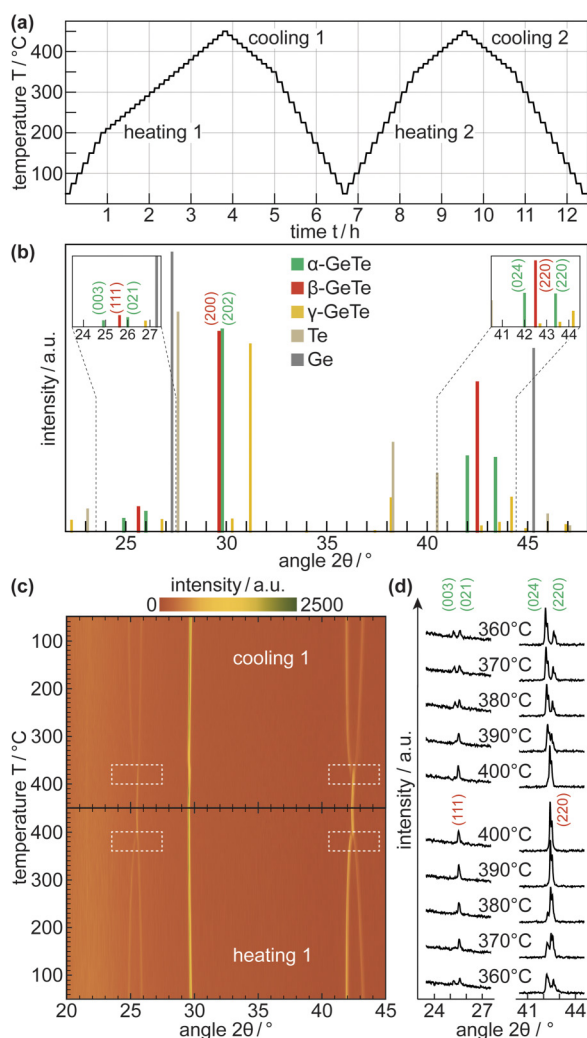
FIG. 2. (a) XRD chamber temperature T as a function of the time t during two heating and cooling cycles with $\vartheta = 10\,°C/\text{min}$ for heating and cooling. (b) Reference XRD patterns for all crystalline GeTe phases, tellurium, and germanium.[31–35] The insets show the angular ranges and Miller indices that allow for a distinction between α- and β-GeTe. Note that the Miller indices of the R3m space group are reported using a hexagonal coordinate system. (c) The *in situ* XRD pattern of flakes from a crystalline GeTe sputter target shows the transition from α- to β-GeTe during the first heating cycle and back to α-GeTe during the following cooling (the relevant temperature ranges are marked by white dashed rectangles). (d) The individual XRD patterns corresponding to the 2θ- and T-range of the α-to-β transition show the peak doublets and singlets with the reflexes marked in green and red, respectively.

structures and the corresponding reference patterns of GeTe are given in Table II and Fig. 2(b), respectively. Additionally, the reference patterns of crystalline Te and Ge, which are known impurities observed in GeTe,[4,20,21] are shown.

During the first heating, we collected an XRD pattern every 25 °C for $T \le 200\,°C$ and every 10 °C for

TABLE II. Overview of the crystalline phases observed for bulk GeTe. As mentioned in Sec. I, α- and γ-GeTe are stable at room-temperature, while β-GeTe is the high-temperature phase.

Phase	Crystal system	Space group no.	Space group	Reference
α	Trigonal	160	R3m	31
β	Cubic	225	Fm$\bar{3}$m	32
γ	Orthorhombic	62	Pnma	33

$200\,°C < T \le 450\,°C$. This was based on prior knowledge of the crystallization with $T_{C,1} > 200\,°C$ observed for small nanoparticles (cf. Table I) and the α-to-β transition $T_{C,2} < 400\,°C$ as reported for bulk GeTe.[2] Since we focused on monitoring the reversible crystalline-to-crystalline transition and no further events were expected for GeTe at lower temperatures during repeated cooling and heating, we adapted our temperature intervals accordingly. Thus, we chose $\Delta T = 10\,°C$ for $450\,°C \ge T \ge 350\,°C$ and $\Delta T = 25\,°C$ for $T < 350\,°C$.

For a reference value regarding the α-to-β transition temperature of bulk GeTe, we characterized flakes of a crystalline GeTe sputter target with *in situ* XRD as described above. The temperature-dependent diffractograms are shown in Fig. 2(c). The transitions from a peak doublet to a single peak for both $2\theta = 24 - 27°$ and $2\theta = 41 - 44°$ allow for the confirmation of the β phase of GeTe. Based on the XRD scans taken every 10 °C, $T_{C,2}$ is extracted as 380 °C [Fig. 2(d)]. This matches the transition temperature of GeTe with a Te content between 50.2 and 50.5% given by the phase diagram in Ref. 2. Hence, we can conclude that the reference sample is stoichiometric.

III. RESULTS AND DISCUSSION

In the following, we will discuss the temperature-dependent XRD patterns for three nanoparticle-based samples. First, we will focus on the structural evolution of the GeTe particles from synthesis 1, which showed a broad size distribution. Second, we will analyze the diffractograms obtained for the particles from synthesis 2, which had a narrower size distribution. Also, it provided two samples with sizes smaller and larger than the average size of the particles from synthesis 1.

All diffractograms were normalized by dividing the intensity values by the maximum intensity for each particular diffractogram, meaning $I/I_{\max}$, which allows for a better graphical representation. Additionally, the patterns are displayed with a constant offset [$(I/I_{\max})+ 0.25$ between each diffractogram] to show the structural evolution of the sample over time. Such waterfall plots facilitate the interpretation of temperature-dependent XRD data since interpolation as used in 2D contour plots [cf. Fig. 2(c)] is avoided. Nevertheless, it has to be noted that the time axis has been adapted to follow the XRD patterns. Thus, the spacing is not necessarily equal. This is due to the fact that we chose $\Delta T = 25\,°C$ for $T \le 200\,°C$ between each measurement in heating 1 as well as for $T \le 350\,°C$ in cooling 1, heating 2, and cooling 2. For higher temperatures in each cycle, we chose $\Delta T = 10\,°C$ for a better
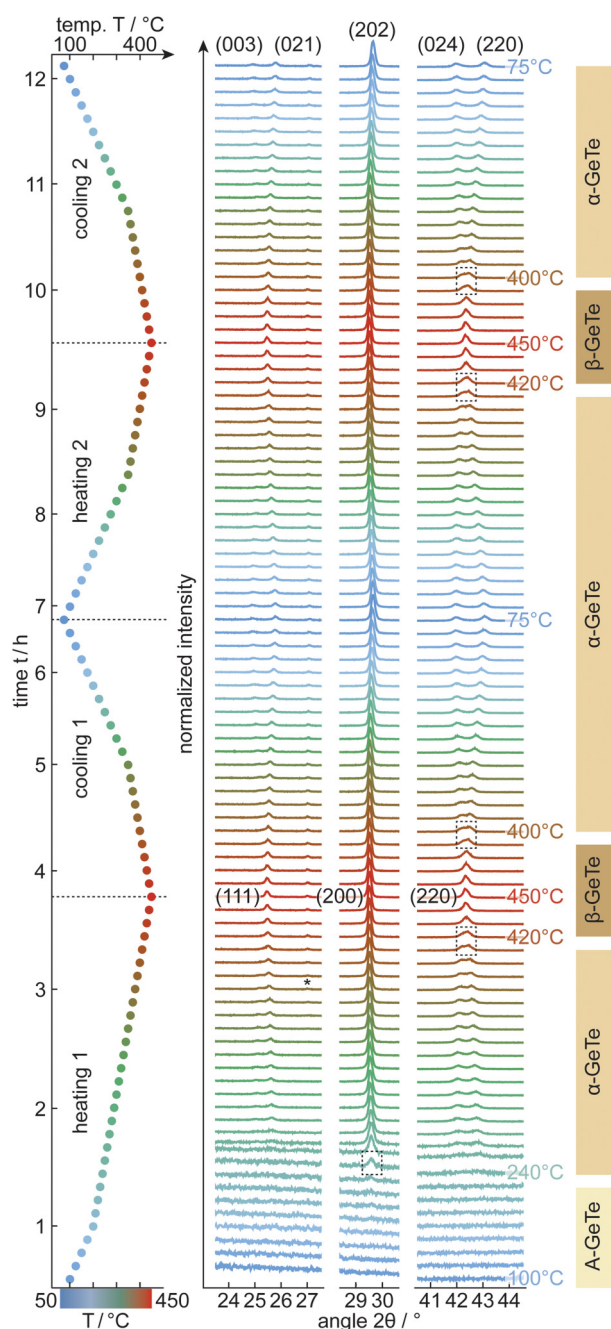
FIG. 3. Structural evolution of GeTe nanoparticles from synthesis 1 with a diameter of 5.5 ± 1.6 nm [green histogram in Fig. 1(f)]. Each XRD pattern is normalized to the maximum peak intensity (I/I_{max}). The colors represent the scan temperature T, as shown on the left side. Upon heating, amorphous GeTe (A-GeTe) crystallizes into α-GeTe, $T_{C,1} = 240$ °C and relaxes into the β-phase. The transition between α- and β-GeTe continues during further heating and cooling with $T_{C,2} = 420$ °C and $T_{C,2'} = 400$ °C. The small peak at $2\theta \approx 27$° (black asterisk) could indicate a small amount of crystalline Te or Ge impurity, cf. Fig. 2(b).

resolution. These temperature choices were defined by the expected structural transitions (cf. Table I).

In the discussion of all temperature-dependent XRD diffracto-grams, we focus on three angular ranges of 2θ to investigate $T_{C,1}$ and $T_{C,2}$,

- $24 - 27$°: transition from (003)/(021)-doublet to (111)-singlet marks α-to-β transition (and vice versa),
- $29 - 30$°: appearance of (202)-peak marks crystallization, and
- $41 - 44$°: transition from (024)/(220)-doublet to (220)-singlet marks α-to-β transition (and vice versa).

Since the doublet-to-singlet transition is more pronounced between 41° and 44° [cf. reference in Fig. 2(b)], we use this angular range to identify $T_{C,2}$. The transition temperatures are marked by dashed rectangles in Figs. 3–5, and the values for $T_{C,1}$, $T_{C,2}$, and $T_{C,2'}$ are noted next to the pattern. $T_{C,2}$ refers to the α-to-β transition during heating, and $T_{C,2'}$ refers to the reverse transition, β to α, during cooling.

For orientation, all diffractograms we will discuss below are color-coded with respect to the heating curve and the temperature scaling. In addition to the transition temperatures $T_{C,1}$, $T_{C,2}$, and $T_{C,2'}$, we mark the transition points between each cycle, i.e., $T_{min} = 75$ °C and $T_{max} = 450$ °C on the right of the XRD patterns.

A. *In situ* XRD on polydisperse GeTe nanoparticles

The diffractograms of the GeTe nanoparticles from synthesis 1, which led to a broad size distribution [cf. Fig. 1(f)], are shown in Fig. 3. The XRD patterns start at $T = 100$°C in the first heating cycle. During heating 1, a narrowing of the intensity peak close to $2\theta = 30$° as well as a convergence of the (024)/(220)-doublet can be seen. First, we focus on the interpretation of the width of the (202) and (200)-peak of the α and β phase, respectively. In a general and simplified consideration, the full width at half maximum (FWHM or w) of an XRD peak can be related to the lattice strain and the crystallite size D. It has to be noted that D is not necessarily identical with the particle size d. In the case of coalescence, for example, D can be larger than the initial d. Hence, without a high-resolution TEM investigation, it is difficult to judge whether the particle or domain sizes are determined via XRD. This ambiguity has to be kept in mind when the term *crystallite* is used for D.[36] Nevertheless, its size can theoretically be estimated from the well-known Scherrer equation,

$$D = [K \cdot \lambda]/[w \cdot \cos(\theta)], \quad (1)$$

with K being the shape factor or Scherrer constant (often approximated by 0.9), λ being the x-ray wavelength in nm, and θ being the angle of diffraction in rad.[36] The observed peak width w_{obs} in rad has to be corrected by subtracting the instrumental broadening w_{instr} in rad,

$$w^n = w_{obs}^n - w_{instr}^n, \quad (2)$$

with n being dependent on the peak shape. In our case, $w_{instr} \approx 0.1$° (determined with a crystal silicon standard) and thus, up to 72% of w_{obs}. Therefore, it would be necessary to collect the
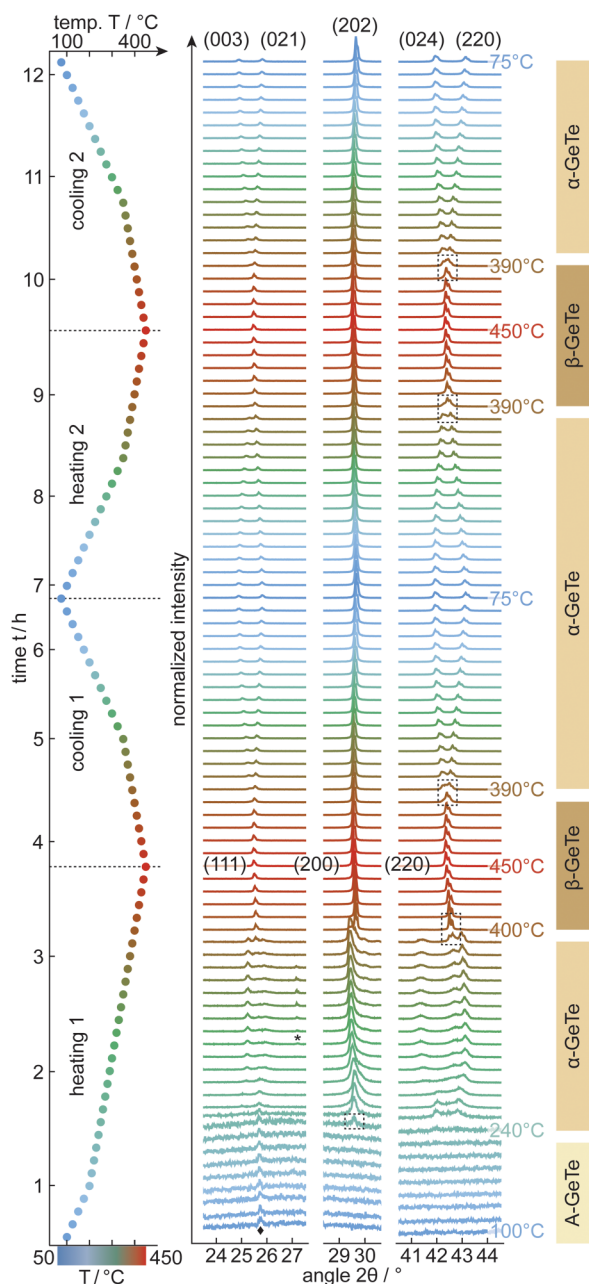
FIG. 4. Structural evolution of A-GeTe nanoparticles prepared by synthesis 2 and with a diameter of 4.8 ± 0.6 nm [blue histogram in Fig. 1(f)]. Normalization, temperature profile, and color code are similar to Fig. 3. Upon heating the A-GeTe nanoparticles, they crystallize into α-GeTe at $T_{C,1} = 240\,°$C and relax into the β-phase at $T_{C,2} = 400\,°$C. The transition between α- and β-GeTe continues during further heating and cooling with $T_{C,2} = T_{C,2'} = 390\,°$C. We ascribe the small peak at $2\theta \approx 27.2°$ (black asterisk) to a small amount of crystalline Te or Ge impurity, cf. Fig. 2(b). The small peak at $2\theta \approx 25.7°$ (black rhombus) could not be matched with any reference diffractograms given (cf. Appendix B). However, graphitic carbon shows a strong peak at this angle and could have contaminated the sample.

diffractograms with a much higher resolution (e.g., at a synchrotron) to obtain a better estimate of D. Nevertheless, a qualitative approximation of D based on the XRD patterns is possible. In a simplified picture, the initial particle diameter $d \approx 5.5$ nm determined by TEM would imply $w_{obs} \approx 1.6°$ (assuming $D = d$, $K = 0.9$, $w_{instr} = 0.1°$, and $\lambda = 0.154\,06$ nm). In contrast, Fig. 3 shows $0.14° \leq w_{obs} \leq 0.2°$. For a conservatively chosen $n = 2$, we can estimate, e.g., $d \approx 49$ nm (Fig. 3, $T_{C,1} = 240\,°$C: $2\theta = 29.6°$, $w_{obs} \approx 0.19°$, cf. Table III). Thus, it seems very likely that the GeTe nanoparticles coalesced during the initial crystallization. Thereby, it has to be emphasized that XRD patterns represent only an averaged signal, and no conclusion on the individual particles can be drawn.

Between $T = 240$ and $300\,°$C, the peak width decreases further, indicating continued growth of D. This could relate to further coalescence or growth of larger grains at the expense of smaller ones.[21,26] Further thermal treatment showed no influence on the width of the (202)- or (200)-peak of α- or β-GeTe, respectively. Thus, it can be assumed that the grain growth stopped. Apart from the narrowing of the (202)-peaks, a slight shift to smaller angles upon heating can be seen. During cooling, the peak position shifts back to its initial value. A similar behavior can be seen for the second heating and cooling. This can be rationalized by the relaxation of the distorted α-phase to the cubic β-phase.[26,37]

For $T = 260\,°$C, the (024)/(220)-doublet becomes clearly visible and converges smoothly toward the (220)-singlet for increasing $T \geq 360\,°$C. This indicates a slow transition from the rhombohedrally distorted α-phase to the relaxed cubic β-phase. Something similar has been observed for larger GeTe nanoparticles, which were crystalline after synthesis.[26] During the first cooling cycle, the gradual splitting of the (220)-peak toward the (024)/(220)-doublet can be seen. The related β-to-α-transition temperature was $T_{C,2'} = 400\,°$C according to the diffractogram. A similar behavior can be found for heating and cooling 2, where the (024)/(220)-doublet transitions into the (220)-singlet at $T_{C,1} = 420\,°$C and the high-temperature phase transitions back into the room-temperature phase at $T_{C,2'} = 400\,°$C. Thus, the transition between the two C-GeTe phases is reversible for the sample based on nanoparticles from synthesis 1.

The aforementioned reversible change is less evident for the (003)/(021)-doublet to (111)-singlet transition at $2\theta = 24-27°$. This was expected due to the low intensity of these peaks in the reference [cf. Fig. 2(b)]. Nevertheless, the transition is visible but does not allow for a determination of the transition temperatures $T_{C,2}$ and $T_{C,2'}$.

B. *In situ* XRD on nanoparticles with narrower size distribution

In Figs. 4 and 5, the diffractograms of the nanoparticles from synthesis 2 are shown. These two samples had a smaller and larger average size and a narrower size distribution than the GeTe nanoparticles discussed in Sec. III A.

While the XRD patterns were collected, normalized, and plotted similarly to Fig. 3, it is obvious that the diffractograms in Figs. 4 and 5 for the amorphous samples with $100\,°$C $\leq T \leq 250\,°$C are noisier. One possible reason could be that the total amount of sample from synthesis 2 was lower
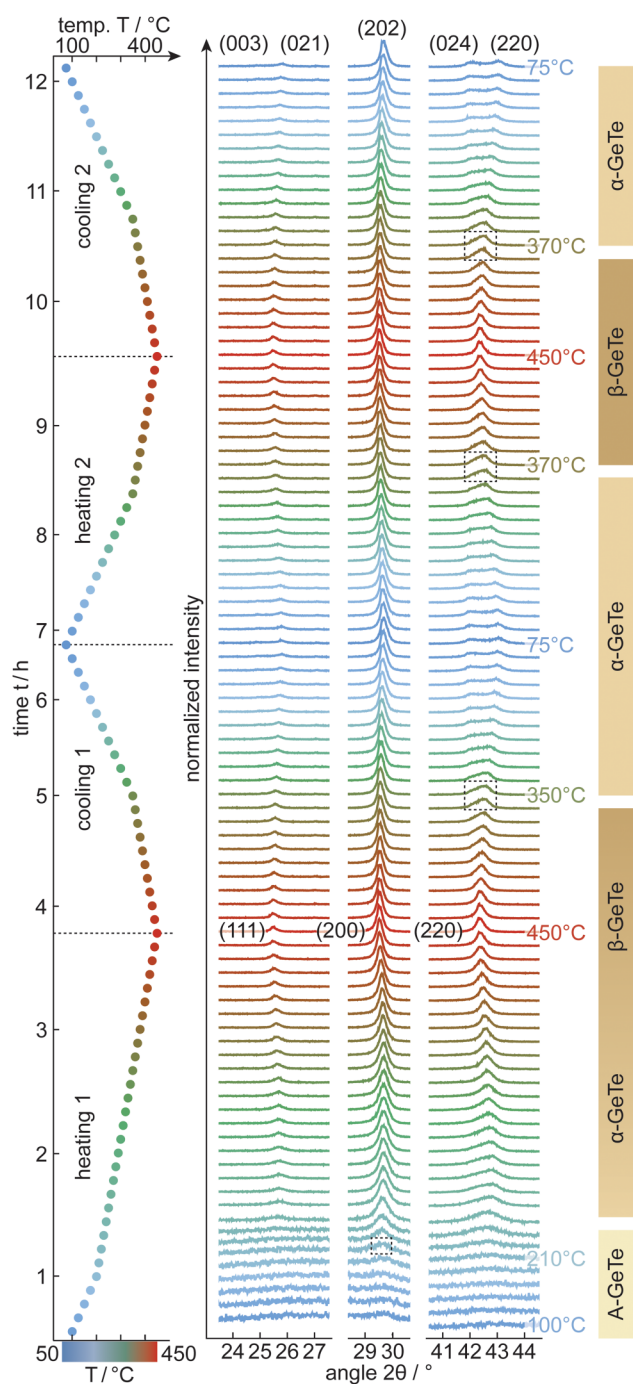
FIG. 5. Structural evolution of A-GeTe nanoparticles from synthesis 2 with a diameter of 6.9 ± 0.9 nm [red histogram in Fig. 1(f)]. Normalization, temperature profile, and color code are similar to Figs. 3 and 4. Upon heating, A-GeTe crystallizes at $T_C = 210\,°C$. Presumably, α-GeTe relaxes into β-GeTe since the transition back to the α phase can be found at $T_{C,2'} = 350\,°C$. During further heating and cooling the crystalline-to-crystalline transitions can be found at $T_{C,2} = T_{C,2'} = 370\,°C$.

compared to samples from synthesis 1 due to different sample contributions from the TOP and oleic acid ligands (cf. Sec. II A). Another reason could be the normalization I/I_{max}. This leads to a pronounced increase of the signal-to-noise ratio (SNR) for XRD patterns above $T_{C,1}$, where $I_{max} \gg I$, but does not affect the SNR of amorphous diffractograms (cf. Appendix A).

In Fig. 4, the first sign of crystallization into α-GeTe can be observed for $T = 240\,°C$, which matches what we already observed in Fig. 3. Again, the peak width indicates a coalescence of particles prior to or during crystallization. Already the XRD pattern for the next temperature step shows a clear (024)/(220)-doublet. Further heating leads to a quick divergence of the two peaks, while the high-angle peak seems to overlap with another small peak. At the same time, the (202) peak shifts quite strongly to lower angles and a weak (003)/(021)-doublet becomes visible. The latter shows a prompt divergence and an overlapping additional peak (for $T = 370 - 390\,°C$) as well. The described trends remain for all three diffractive signatures of the α-phase until $T = 400\,°C$. For this temperature, a prompt shift of the central peak occurs and both doublet-to-singlet transitions are observed. Thus, we define the onset of the α-to-β-transition at $T_{C,2} = 400\,°C$. Further heating leads to a relaxation of the peaks and the subsequent cooling shows the smooth and reversible transition between β- and α-GeTe. This behavior is similar to what was seen in Fig. 3. Only the transition temperatures are slightly lower with $T_{C,2'} = 390\,°C$ and $T_{C,2} = T_{C,2'}$ from there on.

It has to be noted that the (024)/(220)-doublet shows very small split peaks. This could be related to the fact that we used $CuK_{\alpha,1}$ and $CuK_{\alpha,2}$. Since the peaks are sharper compared to what we found for the diffractograms in Fig. 3, this effect might appear more strongly for the sample investigated here. Furthermore, the narrower peaks shown in Fig. 4 indicate a larger crystallite size D and thus, more pronounced coalescence than observed for the GeTe particles from synthesis 1 can be assumed. This is surprising since oleic acid ligands are used for the particles from synthesis 2. These molecules are much longer than the TOP ligands, which are shown in Fig. 1(c), and thus, a more pronounced nanoparticle separation and potentially less coalescence could be expected.[21]

Similar to the diffractograms in Fig. 3, a small additional peak not matching the α- or β-lattice was found. It appears at $2\theta \approx 27.2°$ for $T \geq 310\,°C$, but it disappears for $T \geq 380\,°C$ and does not reoccur throughout the following temperature treatment. Due to the angular position of this peak, it could indicate traces of crystalline Te or Ge in the sample. Since the most pronounced peaks for both crystalline patterns are almost overlapping [cf. Fig. 2(b)], an unambiguous identification is not possible. Nevertheless, Te impurities have been reported for annealed initially amorphous GeTe nanoparticles.[20] Additionally, segregated Te has been observed as a result of surface oxidation of GeTe (cf. Appendix B).[28]

In Fig. 5, a very weak crystalline signal can already be identified for $T = 100\,°C$. The (202)-peak is very broad and flat, thus indicating a much smaller D than what we found for the smaller GeTe nanoparticles (cf. Figs. 3 and 4). Due to this initial (partial) crystallization of the particles, the determination of $T_{C,1}$ is difficult. Therefore, we use the enhancement of this hump at $2\theta \approx 29.6°$,

and the simultaneous onset of a crystalline signal in the high-angle range, which we define for $T_{C,1} = 210\,°C$. However, this is less reliable than $T_{C,1}$ defined for the samples based on the smaller GeTe nanoparticles discussed above.

Further heating leads to more pronounced peaks for the three considered angular ranges. Thereby, the (202)-peaks narrow, while the peak width w_{obs} remains relatively broad compared to what is shown in Figs. 3 and 4. This would imply that coalescence did not progress as far as for these samples. If we could apply the simplified logic of longer ligands resulting in a lower degree of particle sintering, we would expect $D_{5.5} > D_{6.9}$ (particles with an average diameter $d \approx 5.5\,nm$ and TOP ligands vs particles with $d \approx 6.9\,nm$ and oleate ligands).

Similar to what we observed before, the (202)- and (200)-peak, respectively, shift smoothly. However, during the first heating, we cannot determine $T_{C,2}$. Instead, during cooling a broadening and subsequent peak splitting from the (220)-singlet to the (024)/(220)-doublet can be observed, starting at $T_{C,2'} = 350\,°C$. The following α-to-β-transition sets in at $T_{C,2'} = 370\,°C$ with the transition back to α at the same temperature during the second heating cycle. The (003)/(021)-doublet cannot be observed before the end of the last cooling, i.e., $T = 75\,°C$.

IV. CONCLUSION

We synthesized ultrasmall nanoparticles of the phase-change material GeTe with diameters below 10 nm. In the literature, these sizes have been identified to show size-dependent material properties. We studied the crystallization behavior of drop-casted nanoparticle films using *in situ* XRD while heating the films under a nitrogen atmosphere. All nanoparticle-based samples showed crystallization to α-GeTe followed by a crystalline-to-crystalline transition to the high-temperature β-phase of GeTe. During cooling, this transition was reversible and could be repeated for a second heating and cooling cycle. All samples showed increased crystallization temperatures $T_{C,1}$ and $T_{C,2}$ compared to bulk GeTe.

Figure 6 compares our results to the values obtained by previous studies (cf. Table I). While we observed coalescence, similar to the literature, we list the transition temperatures as a function of the initial particle size d. Figure 6 reveals that the literature values follow a general trend of an increasing $T_{C,1}$ and $T_{C,2}$ for decreasing d below 10 nm. However, quantification of the size-dependent $T_{C,1}$ and $T_{C,2}$ is complicated by coalescence. Thus, we propose to perform a similar study with separated nanoparticles, e.g., by using atomic layer deposition. Additionally, the investigation of the temperature-dependent structural transitions with nanoparticles of similar size but passivated with different ligands could allow for a more in-depth coalescence study. Furthermore, *in situ* TEM, *in situ* Raman spectroscopy, and ultrafast DSC could give further insights into the crystallization of individual nanoparticles.[26,38,39] This would be especially interesting for GeTe, since a decrease of $T_{C,1}$ has been found for decreasing particle size d for $Ge_2Sb_2Te_5$, which is one of the most prominent phase-change materials.[10,40] In contrast, Ref. 41 reported an increased $T_{C,1}$ for sputter-deposited doped GeSb, Sb_2Te, and $Ge_2Sb_2Te_5$ films with thicknesses $t < 10\,nm$. Nevertheless, Ref. 42
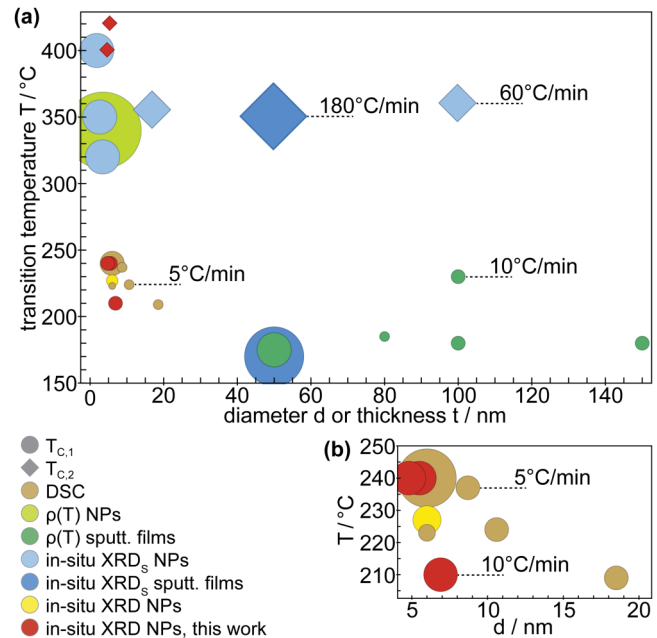
FIG. 6. (a) Comparison of the GeTe transition temperatures $T_{C,1}$ (disk) and $T_{C,2}$ (diamonds) determined for different particle sizes d and film thicknesses t. The colors represent the different characterization techniques and samples. The larger the symbol area, the higher was the applied heating rate ϑ. Exemplary values of ϑ are noted in the plot. (b) A magnified plot for the section in (a) where most $T_{C,1}$ were determined for small d.

showed for $Ge_2Sb_2Te_5$ that this behavior could be ascribed to (capping-dependent) strain in the thin films. The crystallization of nanoparticles will likely be influenced by the large surface-to-volume ratio and presumably, significant strain. Moreover, Kolb *et al.* reported on the nucleation of non-oxidized bulk GeTe at 230 °C. In this context, the crystallization at 180 °C was found to be induced by surface oxidation and related elemental segregation, which led to Te serving as nucleation sites.[28]

Apart from the initial crystallization, our study focused on the reversible α-to-β-transition, which we observed for the three nanoparticle-based samples. These particles were initially amorphous, synthesized following two different protocols, and had different diameters. The α-to-β-transition temperatures were higher compared to the thin films and larger crystalline nanoparticles discussed in the literature (cf. Table I). It is promising that samples based on very small solution-deposited amorphous nanoparticles still show reversible phase-change behavior along with an increased bandgap and tunable refractive index.[23] Although more studies are necessary regarding reproducibility and upscaling, our results show that such nanoscale phase-change materials could be potentially useful for the scalability of active photonics, phase-change random access memory, and optical data storage.

ACKNOWLEDGMENTS

APPENDIX A: FULL-RANGE XRD DIFFRACTOGRAMS

For comparison, the full XRD patterns are shown for exemplary temperatures in Fig. 7 with Fig. 7(a) related to Fig. 3, Fig. 7(b) related to Fig. 4, and Fig. 7(c) related to Fig. 5. The XRD diffractograms are shown for

- 50 °C, which is the lowest T for which XRD was conducted,
- the respective $T_{C,1}$,
- 320 °C for α-GeTe related to heating 1,
- the respective $T_{C,2}$, if applicable,
- 450 °C, which is the highest T for which XRD was conducted, and
- 75 °C for α-GeTe after cooling 1.

In Figs. 3–5 and 7, the diffractograms collected at $T = 50\,°C$ show an amorphous halo at about 22° and 27° for synthesis 1 and 2, respectively. The halo at $2\theta = 22°$ can be related to the quartz substrate as shown in Fig. 8. We ascribe the halo at 27° to the nanoparticles from synthesis 2, for which a similar halo has been observed.[21]

As discussed earlier, we ascribe the initial appearance of a small peak at about 29.6° to the onset of the nanoparticle film crystallization. For clarity, the appearance of this (202)-peak is marked by a dashed rectangle in each diffractogram.

APPENDIX B: IDENTIFICATION OF XRD PEAK AT $2\theta \approx 25.7°$

Considering the particles right after synthesis, the XRD patterns in Fig. 4 show a small peak at $2\theta \approx 25.7°$. According to the potential reference patterns, this would only match β-GeTe which can be excluded as this phase is expected only at higher temperatures. Furthermore, it has been reported that oxidation and segregation can be expected for annealed GeTe.[28] To prevent this, synthesis and XRD measurements were performed oxygen-free. Nevertheless, if oxygen had been present (at elevated temperatures), only amorphous GeO_x and crystalline Te would be expected.[28] The small initial XRD peak at about 25.7° cannot be explained by this. Another possibility could be residual germanium diiodide, which is used as precursor in the synthesis. However, the strongest XRD peaks would be expected at $2\theta \approx 30.4°$ and 26.2° according to Ref. 43.
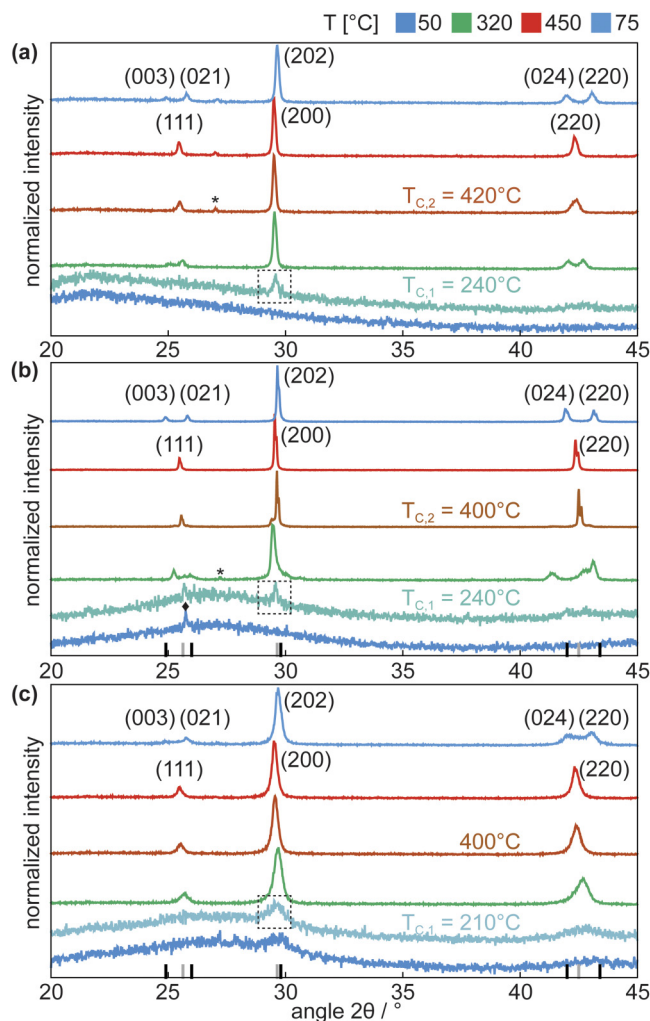

FIG. 7. Diffractograms of A-GeTe nanoparticles shown in (a) Fig. 3, (b) Fig. 4, and (c) Fig. 5 for the full angular range of detection. The normalization and color code are similar to Figs. 3–5. The Miller indices are noted next to the peaks. The reference patterns for α- and β-GeTe are marked in black and gray, respectively, at the bottom of each subfigure. Additional features are marked similarly to Figs. 3 and 4: (a) and (b) black asterisk for Te or Ge impurities, and (b) black rhombus for an unidentified small peak, potentially associated with graphitic carbon. The feature ascribed to the onset of crystallization is marked by a dashed rectangle.

APPENDIX C: ESTIMATION OF CRYSTALLITE SIZE D

By evaluating Eq. (1) under a few assumptions, the crystallite size D can be approximated, as listed in Table III. There, the first heating cycle has been considered. The increase of the crystallite size upon crystallization is expected due to the grain growth. While the Scherrer evaluation has its inherit limitations,[36] further characterization of reproduced nanoparticle syntheses would be necessary for drawing systematic conclusions.
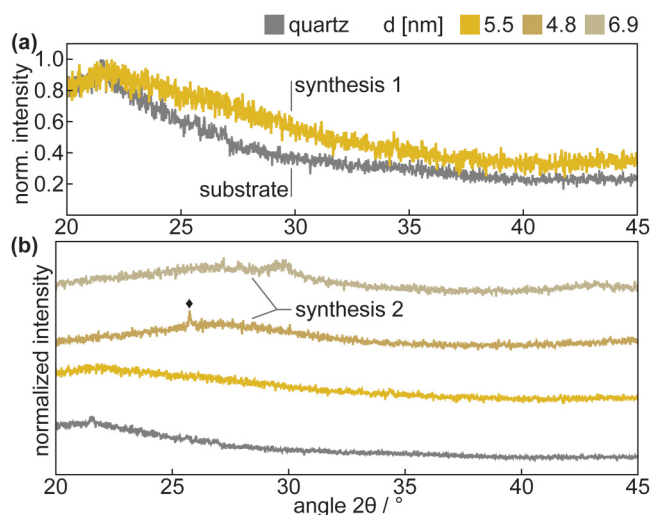
FIG. 8. Diffractograms for the used quartz substrate (gray) and A-GeTe nanoparticles from both syntheses (yellow and beige tones). (a) The empty and loaded quartz substrate are compared. (b) The substrates loaded with the different freshly-synthesized nanoparticles (offset "+1" between each) are compared to the quartz. The black rhombus could potentially be associated with graphitic carbon [cf. Fig. 7(b)].

TABLE III. Estimated crystallite size following Scherrer equation [Eq. (1)] with $n = 2$ and assuming $D = d$, $K = 0.9$, $w_{instr} = 0.1°$, and $\lambda = 0.15406$ nm.

Diffractograms	T (°C)	2θ (deg)	w_{obs} (deg)	d (nm)
Fig. 3	240	29.58	0.19	49
	300	29.55	0.15	72
Fig. 4	260	29.62	0.27	33
	320	29.48	0.20	47
Fig. 5	250	29.67	0.44	19
	300	29.68	0.39	22

DATA AVAILABILITY

The data that support the findings of this study are available from the corresponding author upon reasonable request.

REFERENCES

[1]A. Schlieper, Y. Feutelais, S. G. Fries, B. Legendre, and R. Blachnik, Calphad **1**, 1 (1999).

[2]D. I. Bletskan, J. Ovonic Res. **1**, 53 (2005), see https://chalcogen.ro/Bletskan1.pdf.

[3]J.-Y. Raty, M. Schumacher, P. Golub, V. L. Deringer, C. Gatti, and M. Wuttig, Adv. Mater. **31**, 1806280 (2019).

[4]P. Jost, H. Volker, A. Poitz, C. Poltorak, P. Zalden, T. Schäfer, F. R. L. Lange, R. M. Schmidt, B. Holländer, M. R. Wirtssohn, and M. Wuttig, Adv. Funct. Mater. **25**, 6399 (2015).

[5]The reflectances R_A and R_C were calculated via Fresnel coefficients for a 100 nm GeTe film between a silicon and an air half-space, under normal incidence, and with the dielectric function of GeTe according to Ref. 40. The definition of the reflectance contrast ΔR was taken from Ref. 44.

[6]A. Schlieper and R. Blacknik, J. Alloy Compd. **235**, 237 (1996).

[7]S. Raoux, W. Wełnic, and D. Ielmini, Chem. Rev. **110**, 240 (2010).

[8]C. D. Wright, L. Wang, M. M. Aziz, J. A. V. Diosdado, and P. Ashwin, Phys. Status Solidi B **10**, 1978 (2012).

[9]I. Boybat, M. L. Gallo, S. R. Nandakumar, T. Moraitis, T. Parnell, T. Tuma, B. Rajendran, Y. Leblebici, A. Sebastian, and E. Eleftheriou, Nat. Commun. **9**, 2514 (2018).

[10]M. Wuttig, H. Bhaskaran, and T. Taubner, Nat. Photon. **11**, 465 (2017).

[11]S. G.-C. Carrillo, L. Trimby, Y.-Y. Au, V. K. Nagareddy, G. Rodriguez-Hernandez, P. Hosseini, C. Ríos, H. Bhaskaran, and C. D. Wright, Adv. Opt. Mater. **7**, 1801782 (2019).

[12]C. U. Hail, A.-K. U. Michel, D. Poulikakos, and H. Eghlidi, Adv. Opt. Mater. **7**, 1801786 (2019).

[13]A.-K. U. Michel, S. Meyer, N. Essing, N. Lassaline, C. R. Lightner, S. Bisig, D. J. Norris, and D. N. Chigrin, Adv. Opt. Mater. **9**, e2001243 (2020).

[14]T. Chattopadhyay, J. X. Boucherle, and H. G. von Schnering, J. Phys. C: Solid State Phys. **20**, 1431 (1987).

[15]D. Kriegner, J. Furthmüller, R. Kirchschlager, J. Endres, L. Horak, P. Cejpek, H. Reichlova, X. Marti, D. Primetzhofer, A. Ney, G. Bauer, F. Bechstedt, V. Holy, and G. Springholz, Phys. Rev. B **94**, 054112 (2016).

[16]A. I. Lebedev, I. A. Sluchinskaya, V. N. Demin, and I. H. Munro, Phase Transit. **60**, 67 (1997).

[17]H. Wang, P. Gopal, S. Picozzi, S. Curtarolo, M. B. Nardelli, and J. Sławińska, NPJ Comput. Mater. **6**, 7 (2020).

[18]D. J. Milliron, S. Raoux, R. M. Shelby, and J. Jordan-Sweet, Nat. Mater. **6**, 352 (2007).

[19]H.-S. Chung, Y. Jung, S. C. Kim, D. H. Kim, K. H. Oh, and R. Agarwal, Nano Lett. **9**, 2395 (2009).

[20]M. A. Caldwell, S. Raoux, R. Y. Wang, H.-S. P. Wong, and D. J. Milliron, J. Mater. Chem. **20**, 1285 (2010).

[21]O. Yarema, A. Perevedentsev, V. Ovuka, P. Baade, S. Volk, V. Wood, and M. Yarema, Chem. Mater. **30**, 6134 (2018).

[22]M. J. Polking, P. K. Jain, Y. Bekenstin, U. Banin, O. Millo, R. Ramesh, and A. P. Alivisatos, Phys. Rev. Lett. **111**, 037401 (2013).

[23]A.-K. U. Michel, M. Sousa, M. Yarema, O. Yarema, V. Ovuka, N. Lassaline, V. Wood, and D. J. Norris, ACS Appl. Nano Mater. **3**, 4314 (2020).

[24]O. Yarema, M. Yarema, A. Moser, O. Enger, and V. Wood, Chem. Mater. **32**, 2078 (2020).

[25]I. U. Arachchige, R. Soriano, C. D. Malliakas, S. A. Ivanov, and M. G. Kanatzidis, Adv. Funct. Mater. **21**, 2737 (2011).

[26]M. J. Polking, J. J. Urban, D. J. Milliron, H. Zheng, E. Chan, M. A. Caldwell, S. Raoux, C. F. Kisielowski, J. W. Ager, R. Ramesh, and A. P. Alivisatos, Nano Lett. **11**, 1147 (2011).

[27]S. Raoux, B. Munoz, H.-Y. Cheng, and J. L. Jordan-Sweet, Appl. Phys. Lett. **95**, 143118 (2009).

[28]A. N. D. Kolb, N. Bernier, E. Robin, A. Benayad, J.-L. Rouvière, C. Sabbione, F. Hippert, and P. Noé, ACS Appl. Electron. Mater. **1**, 701 (2019).

[29]R. Mantovan, R. Fallica, A. M. Gerami, T. E. Mølholt, C. Wiemer, M. Longo, H. P. Gunnlaugsson, K. Johnston, H. Masenda, D. Naidoo, M. Ncube, K. Bharuth-Ram, M. Fanciulli, H. P. Gislason, G. Langouche, S. Ólafsson, and G. Weyer, Sci. Rep. **7**, 8234 (2017).

[30]R. C. Keitel, M. C. Weidman, and W. A. Tisdale, J. Phys. Chem. C **120**, 20341 (2016).

[31]J. Goldak, C. S. Barrett, D. Innes, and W. Youdelis, J. Chem. Phys. **44**, 3323 (1966).

[32]L. E. Shelimova, N. K. Abrikosov, and V. V. Zhdanova, Russ. J. Inorg. Chem. **10**, 650 (1965).

[33]S. G. Karbanov, V. P. Zlomanov, and A. V. Novoselova, Dokl. Akad. Nauk SSSR **182**, 832 (1968).

[34]A. J. Bradley, Lond. Edinb. Dublin Philos. Mag. J. Sci. **48**, 477 (1924).

[35]A. S. Cooper, Acta Cryst. **15**, 578 (1962).

[36]F. Girgsdies, "Peak profile analysis in x-ray powder diffraction," in *Modern Methods in Heterogeneous Catalysis Research*, Lecture Series (Department of Inorganic Chemistry, Fritz Haber Institute of the Max Planck Society, Berlin, 2015), see www.fhi-berlin.mpg.de.

[37]J. E. Boschker, R. Wang, and R. Calarco, Cryst. Eng. Comm. **19**, 5324 (2017).

[38]B. Chen, G. H. ten Brink, G. Palasantzas, and B. J. Kooi, Sci. Rep. **6**, 39546 (2016).

[39]J. Pries, S. Wei, M. Wuttig, and P. Lucas, Adv. Mater. **31**, 1900784 (2019).

[40]K. Shportko, S. Kremers, M. Woda, D. Lencer, J. Robertson, and M. Wuttig, Nat. Mater. **7**, 653 (2008).

[41]S. Raoux, J. L. Jordan-Sweet, and A. J. Kellock, J. Appl. Phys. **103**, 114310 (2008).

[42]R. E. Simpson, M. Krbal, P. Fons, A. V. Kolobov, J. Tominaga, T. Uruga, and H. Tanida, Nano Lett. **10**, 414 (2010).

[43]A. S. Avilov and R. M. Imamov, Kristallografiya **13**, 68 (1968).

[44]F. F. Schlich, P. Zalden, A. M. Lindenberg, and R. Spolenak, ACS Photonics **2**, 178 (2015).